Astronomy & Astrophysics manuscript no. output
October 7, 2019
© ESO 2019

Low dust emissivities and radial variations in the envelopes of Class 0 protostars: a signature of early grain growth?

M. Galametz[1], A. J. Maury[1,2], V. Valdivia[1], L. Testi[3,4], A. Belloche[5], Ph. André[1]

[1] AIM, CEA, CNRS, Université Paris-Saclay, Université Paris Diderot, Sorbonne Paris Cité, F-91191 Gif-sur-Yvette, France
e-mail: maud.galametz@cea.fr
[2] Harvard-Smithsonian Center for Astrophysics, Cambridge, MA 02138, USA
[3] ESO, Karl Schwarzschild Strasse 2, 85748 Garching bei München, Germany
[4] INAF ? Osservatorio Astrofisico di Arcetri, Largo E. Fermi 5, 50125 Firenze, Italy
[5] Max-Planck-Institut für Radioastronomie, Auf dem Hügel 69, 53121 Bonn, Germany

Preprint online version: October 7, 2019

ABSTRACT

Context. Analyzing the properties of dust and its evolution in the early phases of star formation is crucial to put constraints on the collapse and accretion processes as well as on the pristine properties of planet-forming seeds.
Aims. In this paper, we aim to investigate the variations of the dust grain size in the envelopes of the youngest protostars.
Methods. We analyze Plateau de Bure interferometric observations at 1.3 and 3.2 mm for 12 Class 0 protostars obtained as part of the CALYPSO survey. We perform our analysis in the visibility domain and derive dust emissivity index (β_{1-3mm}) profiles as a function of the envelope radius at 200-2000 au scales.
Results. Most of the protostellar envelopes show low dust emissivity indices decreasing toward the central regions. The decreasing trend remains after correction of the (potentially optically-thick) central region emission, with surprisingly low $\beta_{1-3mm} < 1$ values across most of the envelope radii of NGC1333-IRAS4A, NGC1333-IRAS4B, SVS13B, and Serpens-SMM4.
Conclusions. We discuss the various processes that could explain such low and varying dust emissivity indices at envelope radii 200-2000 au. Our observations of extremely low dust emissivity indices could trace the presence of large (mm-size) grains in Class 0 envelopes, in which case our results would point to a radial increase of the dust grain size toward the inner envelope regions. While it is expected that large grains in young protostellar envelopes could be built via grain growth and coagulation, we stress that the typical timescales required to build mm grains in current coagulation models are at odds with the youth of our Class 0 protostars. Additional variations in the dust composition could also partly contribute to the low β_{1-3mm} we observe. We find that the steepness of the β_{1-3mm} radial gradient depends strongly on the envelope mass, which might favor a scenario where large grains are built in high density protostellar disks and transported to the intermediate envelope radii, for example with the help of outflows and winds.

Key words. Stars: protostars, formation, circumstellar matter – ISM: dust – Techniques: interferometric – Radio continuum: ISM

1. Introduction

Investigating the properties of dust in the early phases of star formation is essential to understand the physico-chemistry taking place in the collapsing core as well as to trace the pristine properties of the planet forming material building up the protoplanetary disks. From the star-forming cores down to disk scales, the collisions and interactions between grain particles increase and the physical conditions and chemistry evolve, affecting the grain population, their progressive growth and reprocessing. Deriving the dust properties from observations is not trivial. Sub-millimeter and millimeter wavelengths observations of the dust thermal emission have been extensively used to put constraints on the dust opacity. In this regime indeed, the opacity has a strong frequency dependence $\kappa_\nu = \kappa_0\ (\nu/\nu_0)^\beta$, with β the so-called dust emissivity index. Analyzing this dust emissivity index and its variations can help us to probe the grain size distribution (Draine, 2006; Natta et al., 2007; Testi et al., 2014). Works based on PRONAOS, *Herschel*, BLAST, or JCMT measurements have revealed that star-forming clumps present significant variations in their grain emissivity (Chini et al., 1997; Dupac et al., 2003; Martin et al., 2012). No evidence of major grain growth was discovered towards star-forming filament like OMC 2/3 (Sadavoy et al., 2016) or the center of prestellar cores like L1544 (Chacón-Tanarro et al., 2017, 2019), at least at the angular resolution at which these studies were performed. In some Perseus star-forming clumps however, Chen et al. (2016) find dust emissivity indices as low as 1.0 while they have values of about 1.6 in the diffuse interstellar medium (Planck Collaboration et al., 2014; Juvela et al., 2015). These results are in line with models predicting that grain coagulation and the formation of aggregates take place in dense molecular clouds (Ossenkopf & Henning, 1994), the submm/mm emissivity increasing with fluffiness (Bazell & Dwek, 1990; Ossenkopf, 1993). Grain growth processes inside molecular clouds are also required to explain the 'coreshine' phenomenon, a scattering process at 3.6 and 4.5 μm that dominates the absorption (Pagani et al., 2010; Steinacker et al., 2010; Andersen et al., 2013; Lefèvre et al., 2014; Steinacker et al., 2015) and that was first discovered using *Spitzer* observations.

At the other end of the star formation timeline, observations of pre-main-sequence objects (in particular T Tauri stars) with circumstellar disks reveal β values ranging from 2 down to -1 (Beckwith & Sargent, 1991), compatible with the presence of millimeter (Pérez et al., 2012, 2015; Tazzari et al., 2016) and even centimeter grain sizes (Testi et al. (2003); see also models

Table 1. Properties of the sample

Name	α_{2000} [a]	δ_{2000}	Cloud	Dist. [b]	Outflow P.A. [c]	$T_{\rm bol}$ [d]	$L_{\rm int}$ [e]	$M_{\rm env}$ [f]
	[h:m:s]	[°:′:″]		(pc)	(°)	(K)	($L_\odot$)	($M_\odot$)
NGC1333-IRAS2A1	03:28:55.57	31:14:37.07	Perseus	293	+205	41	47	7.9
NGC1333-IRAS4A1	03:29:10.54	31:13:30.98	Perseus	293	+180	29	4.7	12.2
NGC1333-IRAS4B	03:29:12.02	31:13:08.02	Perseus	293	+167	28	2.3	4.7
L1448-2A	03:25:22.40	30:45:13.26	Perseus	293	-63	43	4.7	
L1448-C	03:25:38.87	30:44:05.33	Perseus	293	-17	47	11	1.9
L1448-NB1	03:25:36.38	30:45:14.77	Perseus	293	-80	57	3.9	4.9
SVS13B	03:29:03.08	31:15:51.74	Perseus	293	+167	20	3.1	2.8
L1527	04:39:53.87	26:03:09.66	Taurus	140	+60	59	0.9	1.2
Serpens Main S68N	18:29:48.09	01:16:43.41	Serp. Main	436 [g]	-45	58	11	11
Serpens Main SMM4	18:29:56.72	01:13:15.65	Serp. Main	436 [g]	+30	26	2.2	7.7
Serpens South MM18	18:30:04.12	-02:03:02.55	Serp. South	350 [g]	+188	35	29	5.4
L1157	20:39:06.27	68:02:15.70	Cepheus	352	163	42	4.0	3.0

[a] Peak position of CALYPSO 1.3 mm continuum emission as derived by Maury et al. (2019).
[b] Distance to the hosting cloud. References: Ortiz-León et al. (2018a) for the Perseus sources, Ortiz-León et al. (2018b) for the Serpens Main Cloud, Torres et al. (2009) for L1527, and Zucker et al. (2019) for L1157.
[c] Position angle of the outflow derived from the CALYPSO molecular line emission maps. References: Podio & CALYPSO, in prep and Maury et al. (2019).
[d] Bolometric temperature. References: Motte & André (2001) for IRAS2A1, L1527, and L1157, Enoch et al. (2011) for SerpM-S68N, Kristensen et al. (2012) for SerpM-SMM4, Maury et al. (2011) for SerpS-MM18, Tobin et al. (2016) for SVS13B, and from Sadavoy et al. (2014) for the rest of the sources.
[e] Internal luminosity. The $L_{\rm int}$ were calculated from the analysis of the *Herschel* maps from the Herschel Gould Belt survey (André et al., 2010, ; Ladjelate in prep) and rescaled to the distances used in this analysis.
[f] Envelope mass. References: Enoch et al. (2009) for L1448-2A, Chini et al. (1997) for SVS13B, Karska et al. (2013) for IRAS2A1, Motte & André (2001) for L1527 and L1157, Kaas et al. (2004) for the Serpens Main Cloud sources, Maury et al. (2011) for the Serpens South source, and Sadavoy et al. (2014) for the rest of the sample. The $M_{\rm env}$ were re-scaled to the distances used in this analysis.
[g] A mean distance of 436 pc for the Serpens Cloud has been determined by Ortiz-León et al. (2018b) using the Gaia-DR2 results and seems to correspond to the average distance determined from the Main Cloud or the star-forming region W40. On-going work re-analyzing the Gaia data toward Serpens South seems, however, to suggest a first layer of extinction around 300-350pc while its associated young stellar objects could be distributed in a larger extinction layer up to distances of 350 pc (Palmeirim, André et al. in prep). We use this new distance for the paper. As we are working on flux ratios, this will not affect the slope we present for SerpS-MM18. This, however, has an impact on the envelope mass discussed in Sect. 6, that would be higher by a factor of 1.6 if the distance is 436 pc.

from D'Alessio et al. (2001)). How and when dust grains evolve during the building of the star/disk system, i.e. during the protostellar phase, is less clear. Several analyses, mostly on individual objects, have tried to address these questions. If Agurto-Gangas et al. (2019) find no clear sign of grains larger than 100 μm in the inner envelope of the Class I protostar Per-emb-50, Jørgensen et al. (2007) showed that the inner envelopes of deeply embedded protostars could present dust emissivity indices of $\sim$1 that may be indicative of grain growth in these young objects. No evidence seems to be found yet of an evolution of the grain growth from the inner regions of the envelopes to the planet forming disks (e.g. Ricci et al., 2010; Testi et al., 2014).

Several studies suggest that grain growth could occur even earlier than the Class I phase, i.e. at the Class 0 phase. Class 0 objects are the youngest protostars: most of their mass resides in an extended envelope (with outer radii as large as 10^4 au) that is being accreted onto a protostellar embryo (Andre et al., 1993; André et al., 2000) during very short timescales (t $\leq 5\times10^4$ yr; Maury et al., 2011). Kwon et al. (2009), Chiang et al. (2012), and Li et al. (2017) showed that a dozen of Class 0 protostellar envelopes present β at mm wavelengths lower than 1.7, and for some objects even lower than 1. β values of 1 have been obtained at 1.3 mm from models using grain growth alone (Miyake & Nakagawa, 1993; Ossenkopf & Henning, 1994; Draine, 2006). Many questions remain, however, on how realistic β values lower than 1 are or on how large (mm-size) grains can form in Class 0 envelopes in spite of the long timescales and high densities required to build them. Current radiative transfer models of young protostellar envelopes and disks already try to incorporate variations in the grain composition (e.g. ices) and size distribution (Whitney et al., 2003; Robitaille et al., 2006; Facchini et al., 2017). More observations are, however, needed to put constraints on the dust properties within the protostellar envelopes during the disk-forming stage, that is the Class 0 stage, and to identify the environmental parameters (protostar mass, temperature, hosting cloud conditions) leading to these variations in order to probe the pristine material building up the planet forming disks and build a coherent end-to-end scenario of the grain evolution.

Class 0 protostars are ideal candidates to investigate the potential grain growth processes taking place during the main accretion phase and establish the pristine dust properties from which the future disk originates. In the following work, we aim to perform a resolved and multi-frequency mm analysis of the variations of the dust properties in a sample of 12 Class 0 protostellar envelopes observed as part of the Continuum And Lines in Young ProtoStellar Objects survey (CALYPSO, PI: Ph. André; `http://irfu.cea.fr/Projets/Calypso/`). Interferometric observations at millimeter wavelengths are ideal to perform this analysis: most of the envelope/disk emission is optically thin in this regime, limiting the biases in accessing to the dust opacity and studying its spatial variations. We provide

details on the sample and data reduction in Sect. 2 and analyze the 1 to 3 mm β radial profiles in Sect. 3. We correct our β_{1-3mm} profiles for the central regions in Sect. 4 and describe its implications for our results. We analyze the dust emissivity values and radial gradients and their dependence on the global source properties in Sect. 5. Our results are summarized in Sect. 6.

2. Data

2.1. The sample

The CALYPSO sources have been selected from various nearby (d = 140 − 436 pc) star-forming clouds and observed at 1.3 and 3.2 mm using the IRAM - Plateau de Bure Interferometer (PdBI) (Maury et al., 2019). Both, the most extended configuration (A array) and the intermediate antenna configuration (C array) were used to probe the dust continuum emission over a large range of baselines. For this analysis, we select the 12 brightest protostars of the CALYPSO sample, namely sources with a 1.3 mm PdBI integrated flux higher than 100 mJy (according to Table 4 in Maury et al., 2019). The sample is diverse in terms of morphologies (it includes single objects as well as close and wide binaries), bolometric luminosities (from 1 up to 30 $L_{\odot}$) or bolometric temperatures (from 25 to 60 K). The source characteristics are summarized in Table 1. For further details on the morphology of the dust continuum emission in this sample of sources, we refer to the maps shown in Appendix B of Maury et al. (2019). Maps of the gas kinematics are shown in Gaudel et al. (2019, sub.).

2.2. Data processing

We work on the common range of baselines sampled at both 1.3 and 3.2 mm, thus ranging from 20 to 220 kλ. The data calibration (and self-calibration for some of the sources) was performed with GILDAS[1] using the CLIC (Continuum and Line Interferometer Calibration) package. We refer the reader to Maury et al. (2019) for details on the observations, data reduction, Plummer models fitted to the dust continuum visibility profiles. Figure 1 shows the real part of the visibilities at 1.3 and 3.2 mm (circles and triangles respectively), with baselines averaged every 20 kλ. Errors are estimated by adding in quadrature the calibration uncertainties (∼10% at 94 GHz and ∼15% at 231 GHz) and the rms dispersion around the weighted mean in each bin. Our analysis is restricted to the properties of the dust continuum emission around the primary protostars, as defined in Table 2 of Maury et al. (2019). The two sources L1448-N and L1448-2A host a secondary source that is strongly contributing to the visibility profiles. For these sources, we choose to show only the amplitudes of the shortest baselines derived using the center of the binary system as the phase center and thus tracing the general dust properties in the outer envelope of the binary system. We additionally indicate the fluxes at the ∼200 kλ baseline obtained using the primary source as the phase center in order to show how the dust properties connect between these two scales.

2.3. Free-free + synchrotron contribution

In protostars, thermal (free-free) emission produced by a jet or a photo-evaporative wind (see Anglada et al., 1996; Lugo et al., 2004; Pascucci et al., 2012; Tychoniec et al., 2018a, for observations and theoretical models) as well as, to a lower extent, from non-thermal (synchrotron) emission (André, 1996) originating from the presence of magnetic fields can contribute to the 1-3 mm emission within the central 50 au around the protostar. We estimate the contribution to the 1.3 and 3.2 mm fluxes not coming from thermal dust emission from radio measurements beyond 2 cm. Details for each source are provided in Appendix A. The contribution is systematically lower than 10% at 1.3 mm, but can be non-negligible at 3.2 mm. Correcting for this compact contamination is one of the reasons that motivate the 'central region correction' we apply and discuss in Sect. 4.

2.4. Optically-thick emission at 1.3 and 3.2 mm

If regions of our Class 0 envelopes are optically thick, the intensity should only depend on the temperature of the emitting material and the brightness temperature be equal to the actual temperature in the region. Following Motte et al. (1998), we have:

$$\frac{S_{1.3}}{\Omega} \propto (1 - \exp(-\tau))\, B_{1.3}(T_{\rm dust}) \quad (1)$$

with S the flux density (here taken at 1.3 mm), Ω the solid angle associated with the physical scale probed, τ the optical depth and B the Planck function derived from the dust temperature. The dust temperature is estimated with Eq. 6 (c.f. Sect. 3). If the medium is optically thick, so if tau>1, (1-exp($-\tau$))*B tends toward B. If the medium is optically thin, we should observe S/Ω < $B(T)$. We thus use the radially determined fluxes at 231 GHz maps divided by Ω and compare them to the $B(T)$ profiles.

Figure 2 shows how the two quantities vary with the scales in au. The absence of overlap between the two profiles indicates that most of the continuum emission of the envelope scales we probe is optically thin, except perhaps for the 1.3 mm emission coming from the < 200 au regions of IRAS4A, IRAS4B or SerpM-SMM4. Here again the 'central region correction' applied in Sect. 4 will allow us to correct for the potential central optical thickness effects affecting the visibility profiles.

3. Observational results

An interferometer only samples the uv plane at discrete spatial frequencies. Voids in this under-sampled Fourier space are a challenge for interferometric image reconstruction. We thus decide to perform our analysis of the grain size distribution variations directly in the visibility domain. As described in many analyses (Harvey et al., 2003; Maury et al., 2019, among others), if the density and temperature distributions in the envelope will follow a power law, respectively $\propto r^{-p}$ and $\propto r^{-q}$ (Adams, 1991; Motte & André, 2001), then in the Rayleigh-Jeans approximation, the intensity will follow a power law $I(r) \propto r^{-(p+q-1)}$. The resulting visibility distribution will be a power law as well, expressed as $V(b) \propto b^{(p+q-3)}$. The ratio of the amplitude visibility measured at two wavelengths at a common baseline thus traces the spectral index of the dust composing the emitting material within a given area corresponding to the scale probed by the specific baseline. The variations of the millimeter spectral index β_{mm} can then be used as a signature of variation of the grain size distribution, with lower β values associated to the presence of more emissive grains, as expected for larger grains (Kruegel & Siebenmorgen, 1994).

[1] https://www.iram.fr/IRAMFR/GILDAS/

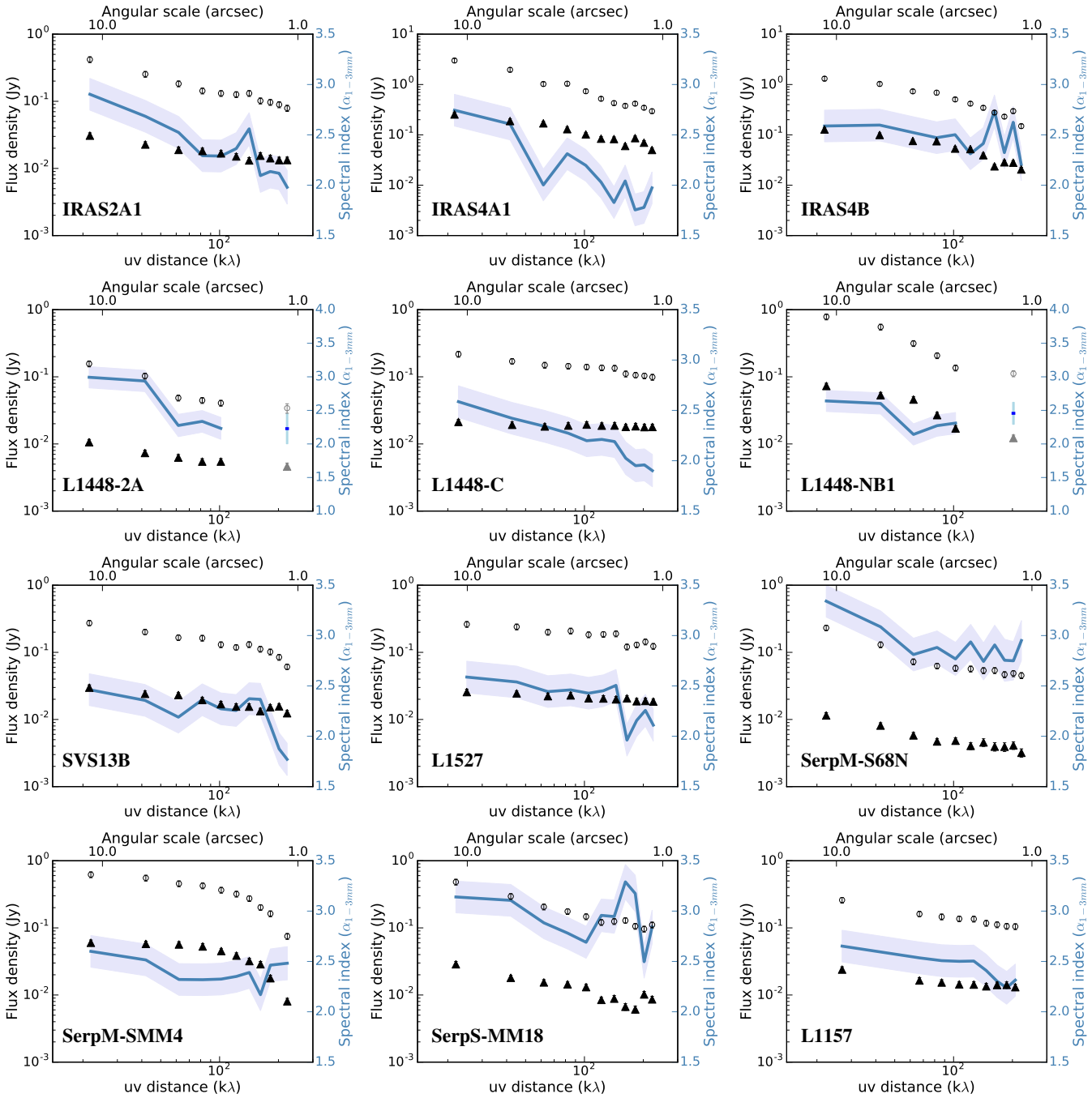

Fig. 1. Continuum flux density at 1.3 mm (open circles) and 3.2 mm (filled triangles) as a function of the baselines averaged every 20 kλ. The variations of the observed spectral index α_{1-3mm} (see Eq. 2) are overlaid (blue line). Their values are shown on the right y-axis. Error bars indicate the flux uncertainties and include the calibration errors. Those are used to derive the uncertainties on α_{1-3mm} shown as the shaded blue area. As L1448-N and L1448-2A host a secondary source, we only show the continuum flux densities at the shortest baselines but also indicate the flux at ~200 kλ obtained using the primary source as the phase center (see Sect. 2.2 for more details).

3.1. Observed spectral index profiles with uv-distance

The dust continuum emission fluxes at 1.3 and 3.2 mm, as measured in bins of baselines, are shown in Fig. 1. The figure also shows the variations of the observed spectral index α_{1-3mm} defined as:

$$\alpha_{1-3mm} = \frac{log(F(\nu_0)/F(\nu_1))}{log(\nu_0/\nu_1)} \quad (2)$$

with ν_0 and ν_1 equal to 231 and 94 GHz respectively. Figure 1 indicates, overlaid on the visibilities, the variations of the observed spectral index α_{1-3mm} (blue lines, scale provided on the right axis) for each object.

In order to express the uv-distances in terms of angular separations, we use the relation linking the brightness distribution I of an object to its complex visibility given by the Fourier transform :

$$I(x,y) = \int_{-\infty}^{\infty}\int_{-\infty}^{\infty} V(u,v)\exp(2\pi i(xu+yv))dudv \quad (3)$$

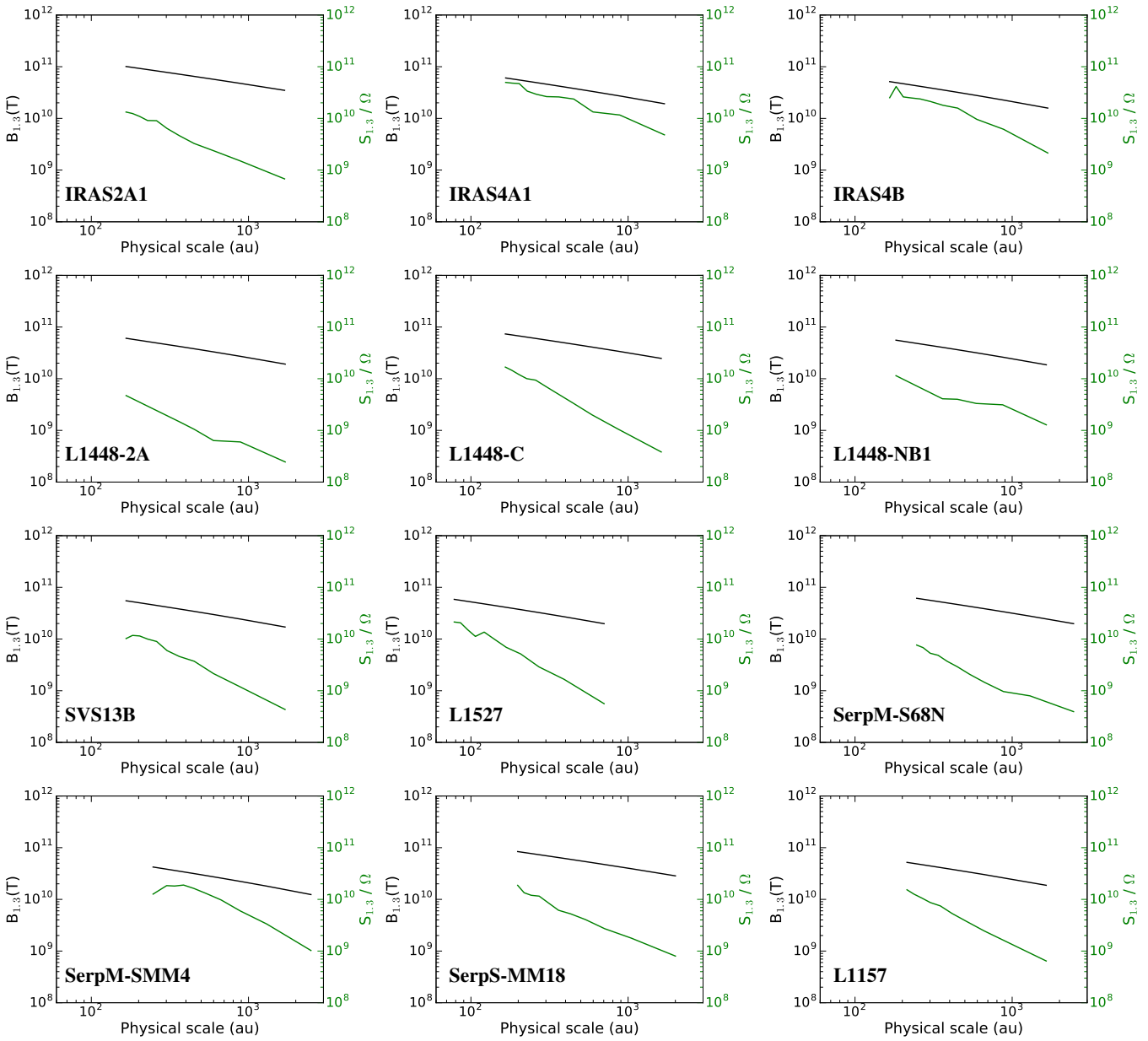

Fig. 2. Comparison between $S_{1.3}/\Omega$ (with S the flux density at 1.3 mm and Ω the solid angle associated with the physical scale probed) and the Planck function profile associated with the dust temperature profile of the envelope. The fact that $S_{1.3}/\Omega < B_{1.3}(T)$ in the objects indicates that the envelopes (at the radii probed by our analysis) can be considered as optically thin.

where (x, y) represent the angular coordinates on the sky (in radians) and (u, v) the coordinates describing the baseline. For an assumed circularly symmetric object, we can use the zeroth-order Bessel function J_0 to write:

$$V(b) = \int_0^{\infty} 2\pi I(\theta) J_0(2\pi\theta b) d\theta \sim \int_0^{x_0/2\pi b} 2\pi I(\theta)\theta d\theta \quad (4)$$

with x_0 the first zero of J_0. The visibility reaches its first zero when $b_{V=0}$=1.22(λ/θ), resulting in a baseline - angular scale relation given by:

$$\theta = 1.22\frac{\lambda}{b} \quad (5)$$

These angular scales θ, over which the dust continuum emission is integrated to compute the spectral index, are indicated on the top axis of Fig. 1. We observe that most of the objects show a clear decrease of the observed spectral index $\alpha_{1-3\mathrm{mm}}$ toward larger uv-distances, thus smaller envelope radii. Several objects of the sample have already been studied using other mm interferometric observations with similar resolutions, allowing us to confront our observations with previous works. L1157 has been studied using CARMA by Kwon et al. (2009) and Chiang et al. (2012) who derived the profile of the dust emissivity index as a function of uv-distance using the Rayleigh-Jeans approximation and the optically thin assumption. Our results are consistent with the relatively flat profile they observe on 10-40 au and 25-2500 au scales respectively: L1157 has one of the weakest gradient of our sample. For L1527, we find a very similar flat profile of the observed spectral index as a function of uv-distance than that found by Tobin et al. (2013).

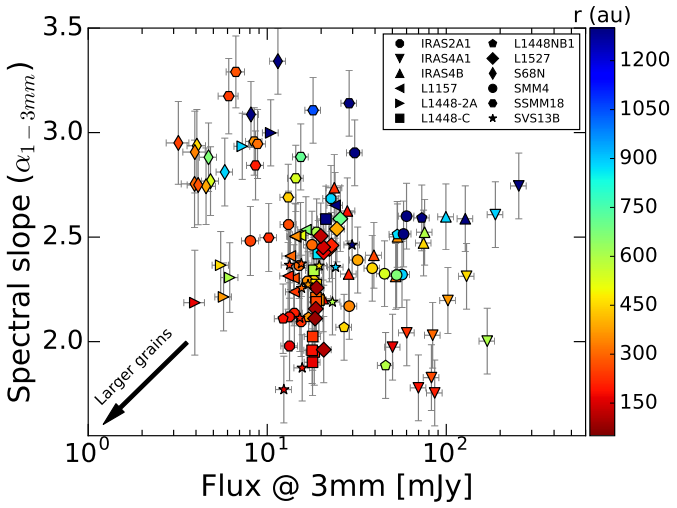

Fig. 3. Variation of the observed spectral index α_{1-3mm} derived in the baseline bins of Fig. 1 as a function of its associated 3.2 mm flux density. Each symbol represents a different protostellar envelope and symbols are color-coded with respect to the physical distances probed (in au). The bottom left arrow indicates the trend predicted when the grain size is increasing (see models from Miotello et al., 2014).

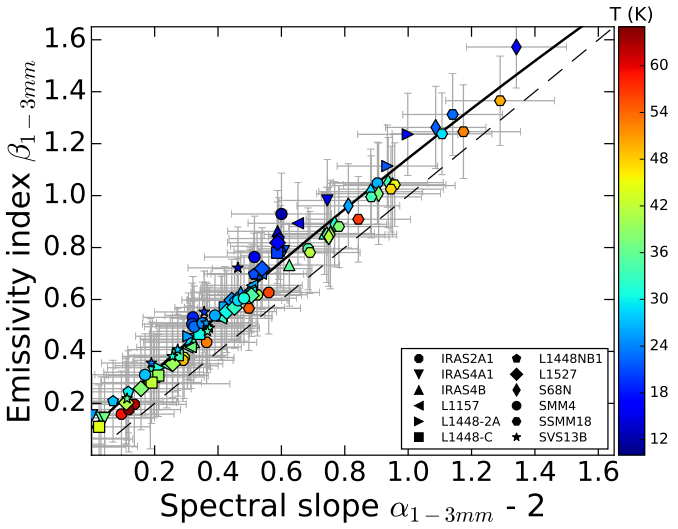

Fig. 4. Relation between the dust emissivity index β_{1-3mm} and the observed spectral index α_{1-3mm}-2. The dashed line represents the 1:1 relation while the plain line represents the polynomial regression to the data (β_{1-3mm} = -0.07 (α_{1-3mm}-2)^2 + 1.12 (α_{1-3mm}-2) + 0.10). Each symbol represents a different protostellar envelope and symbols are color-coded with respect to our modeled dust temperature.

The observed spectral indices derived in baseline bins as a function of their associated 3.2 mm flux densities are shown in Fig. 3. Each point is color-coded as a function of the radius over which the integrated quantities are computed, in au (using eq. 5 and r = $\theta \times d/2$). Miotello et al. (2014) generated a series of families of disk models following the method developed in Testi et al. (2001) to interpret their mm observations of the two Class I protostars Elias29 and WL12. We overlay in the bottom left corner of Fig. 3 the evolution of the grain size expected from these models, even if those do not directly apply to our Class 0 sources. Observationally, the outer regions of our protostellar envelopes populate the upper right part of the plot while the central regions have lower α_{1-3mm} and fluxes, thus are located in the lower left part. As the Miotello et al. (2014) models predict a progressive increase of the grain size as we move from the upper right to the lower left corner of the plot, we conclude that our observations are consistent with the presence of larger grains when probing smaller and smaller scales.

3.2. Dust emissivity index radial profiles

In the Rayleigh-Jeans approximation (and assuming optically thin emission at mm wavelengths), α values translate to a dust emissivity index $\beta = \alpha$-2. This is, however, only a proxy for β as the Rayleigh-Jeans approximation does not hold across protostellar envelopes because of their low dust temperatures. To offer a more robust approximation, we re-calculate β_{1-3mm} assuming that our objects are centrally illuminated spherical envelopes in which the temperature varies with radius (Terebey et al., 1993; Motte & André, 2001) as:

$$T = 38\, L_{\rm int}^{0.2} \left(\frac{\rm r}{100\ {\rm au}}\right)^{-0.4} \quad (6)$$

The protostellar internal luminosities $L_{\rm int}$ (in $L_\odot$) are tabulated in Table 1. We then use the temperature profiles to calculate the binned β values using:

$$\beta = \frac{log((F(\nu_0)/B_{\nu_0}(T))/(F(\nu_1)/B_{\nu_1}(T)))}{log(\nu_0/\nu_1)} \quad (7)$$

with ν_0 and ν_1 equal to 231 and 94 GHz respectively and $B_\nu(T)$ the Planck function. The relation linking the dust emissivity index β to the observed spectral index α_{1-3mm}-2 is shown in Fig. 4. We immediately observe that the relation deviates from the 1:1 relation as one points toward colder regions (with α_{1-3mm}-2 underestimating β at colder temperatures). This has a direct impact on the β_{1-3mm} radial gradients, steepening most of them. For a visual illustration, maps of β_{1-3mm} have been generated from the 1.3 and 3.2 mm dust continuum cleaned maps (see Table C.1 and Appendix C) but we perform the following analysis on the visibility datasets, not on the maps.

Figure 5 (black lines) shows how the dust emissivity index β_{1-3mm} varies within the envelopes for each object of our sample. Our β_{1-3mm} values can be reconnected with those presented in Bracco et al. (2017) on larger scales derived with *Herschel* and NIKA. They found that the emissivity β decreases radially in the two protostellar cores studied in Taurus while staying flat in the pre-stellar core they analyzed, with values of β=1.0-1.5 that nicely match the range of β_{1-3mm} we observe in most of our sources beyond 2000 au. We provide the β_{1-3mm} values we derive at 500 au in Table 2. They range from 0.38 to 0.92. We remind the reader that the typical value found in the diffuse ISM is $\beta \sim$ 1.6 (Planck Collaboration et al., 2014; Juvela et al., 2015). The β_{1-3mm} values observed at 500 au are thus extremely low for the whole sample. If absolute flux calibration does affect the β_{1-3mm} measured, the fact that all sources present low β_{1-3mm} values would imply a systematically under-estimated 1.3 mm flux (or over-estimated 3.2 mm flux) that is not expected since the data comes from > 30 independent tracks observed over a period > 2 years. Phase noise could produce a loss of 1.3 mm flux at long baselines, but this does not affect our analysis here, since we limit ourselves to baselines < 200 kλ, thus recovering the dust continuum emission at envelope scales.

Clear radial variations appear in the envelopes of several objects. To quantify these variations, we fit the β_{1-3mm}-radius trend in lin-log scale and call 'β_{1-3mm} gradient' the slope of the rela-

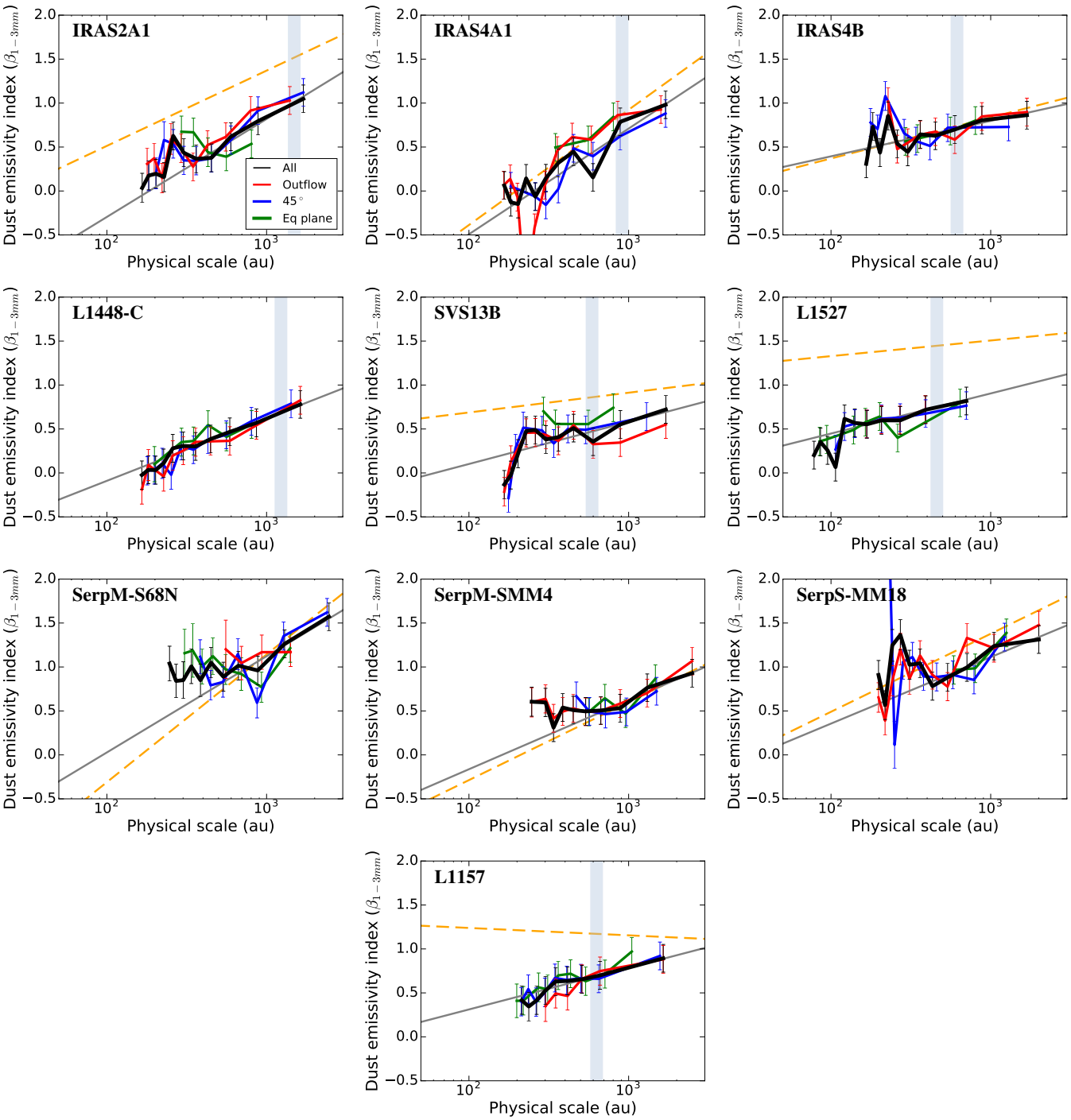

Fig. 5. Variation of the dust emissivity index $\beta_{1-3\mathrm{mm}}$ as a function of the physical scale integrated in the protostellar envelope. The thick black line indicates the trend when all directions are considered while the gray line indicates the (log-lin) fit to the trend (see Table 2). The colored lines indicate the trend in different angular bins with respect to the outflow direction. If PA is the position angle with respect to the outflow axis, the red lines indicate the trends for regions located close to the outflow direction (-22.5° < PA < 22.5°). Blue lines indicate the trends for regions located close to the 45° PA (22.5° < PA < 67.5° and -67.5° < PA < 22.5°). Green lines indicate the trends for regions located close to the equatorial plane (67.5° < PA < 122.5°). The orange dotted line indicates the fit to the β_{1-3mm} values corrected for the central region (see Sect. 4). We do not apply the correction for L1448-C, as its 3mm flux is dominated at most scales by the compact component, with barely any flux coming from the envelope, leading to large uncertainties in the β_{1-3mm} determination. Finally, the light blue shaded line indicates the position of the CO snow line determined from the N_2H^+ and $C^{18}O$ observations (Anderl et al., 2016, and Gaudel et al. in prep).

tion linking beta with the logarithm of the radius (in au):

$$\beta_{1-3\mathrm{mm}} = A\ log(r) + B. \quad (8)$$

with A the $\beta_{1-3\mathrm{mm}}$ gradient. With this definition, A = 2 indicates that $\beta_{1-3\mathrm{mm}}$ doubles its value over an order of magnitude in radius. Gradients are calculated using baselines below 100 kλ to limit the noise present at longer baselines and only probe the dust emissivity variations at envelope scales (i.e. 300 to 4000 au, depending on the source distance). We provide the $\beta_{1-3\mathrm{mm}}$ gradients in Table 2. Some objects show flat $\beta_{1-3\mathrm{mm}}$ profiles, in

Table 2. Emissivity index β_{1-3mm} at 500 au and radial gradients [a]

Name		β_{1-3mm} @ 500 au	β_{1-3mm} gradient
IRAS2A1		0.38 ± 0.16	1.12 ± 0.37
	c.r.c	0.82 ± 0.17	0.86 ± 0.37
IRAS4A1		0.44 ± 0.16	1.21 ± 0.36
	c.r.c	0.54 ± 0.16	1.31 ± 0.36
IRAS4B		0.64 ± 0.16	0.40 ± 0.36
	c.r.c	0.62 ± 0.16	0.46 ± 0.36
L1448-C		0.41 ± 0.16	0.70 ± 0.37
	c.r.c	-	-
SVS13B		0.51 ± 0.16	0.48 ± 0.37
	c.r.c	0.99 ± 0.16	0.22 ± 0.36
L1527		0.73 ± 0.16	0.45 ± 0.40
	c.r.c	1.41 ± 0.16	0.18 ± 0.39
SerpM-S68N		0.92 ± 0.17	1.09 ± 0.38
	c.r.c	0.66 ± 0.27	1.47 ± 0.44
SerpM-SMM4		0.50 ± 0.16	0.79 ± 0.36
	c.r.c	0.44 ± 0.16	0.90 ± 0.37
SerpS-MM18		0.81 ± 0.16	0.77 ± 0.37
	c.r.c	0.74 ± 0.17	0.90 ± 0.37
L1157		0.65 ± 0.16	0.48 ± 0.42
	c.r.c	1.17 ± 0.18	-0.09 ± 0.44

[a] β_{1-3mm} gradients are defined as A so that β_{1-3mm} = A log(r) + B. β_{1-3mm} values at 500 au and gradients are estimated by generating 2000 sets with β_{1-3mm} values varying randomly within their individual error bars (following a normal distribution around their nominal value). Only baselines below 100 kλ are taken into account for the calculation of the gradients. The 'c.r.c' ('central region correction') rows indicate the values when the central regions are removed (see Sect. 4).

particular IRAS4B, SVS13B and L1157. In L1157, Kwon et al. (2015) found that the dust emissivity index changes with radius, with a mean β_{1-3mm} value of 0.76, but values as low as 0.1 at 80 kλ. We do not detect such low values at these scales. Our results are closer to those of Chiang et al. (2012) in that respect, namely that β_{1-3mm} does not vary much depending on the envelope radius in L1157.

3.3. Investigating dust emissivity variations with respect to source morphology

The source physical properties (high densities in the equatorial plane, outflows) could have an impact on the grain populations and thus affect the structure and evolution of the central regions. To analyze potential local variations of the dust emissivity index, we choose to analyze separately the visibilities corresponding to different angular bins. The outflow opening angles are still poorly constrained and can vary significantly from one source to another. In Hsieh et al. (2017), the median opening angle for the outflow of their low-mass objects is 42° (their Table 1). We thus choose to study separately the visibilities in 45^o angular bins, namely *i)* close to the outflow direction, *ii)* close to the equatorial plane or *iii)* close to the ±45° PA. The separation of the visibilities with respect to their uv position angle is performed using the `GILDAS/MAPPING`[2] software. The outflow position angles are provided in Table 1. We plot the radial trends of the dust emissivity located in these different regions in Fig. 5. We do not perform the analysis for L1448-2A and L1448NB1 because they are close binaries driving non-aligned protostellar jets, which confuse the assumption of a simple geometry on the envelope for these sources. We observe that for most of the objects, the trends are similar in all directions. Our data therefore does not point to significantly different dust properties in the outflow direction or the equatorial plane, at least at the 80-2500 au scales we trace in this analysis. While this is surprising at first sight, we stress that such analysis should be repeated on sensitive data probing the dust continuum emission both at the very small and very large envelopes scales, so the outflow cavity walls can be detected and explored individually for example. A better knowledge of the outflow opening angles and orientation would help us refine our crude separation in outflow/equatorial plane regions. We finally note that in L1157, the 3.2 mm emission is more extended than the 1.3 mm emission in the outflow direction (Maury et al., 2019), an elongation also observed at 2.7 mm with PdBI (Beltrán et al., 2004) and 3mm with CARMA (Chiang et al., 2010)[3]. Gueth et al. (1997) suggest that the asymmetry could be linked with an extended component arising from the compressed outflow cavity edges (their Fig. 10). In the visibility plots, we observe that the dust emissivity index seems to be slightly lower in the outflow direction. The trend is also observable in the β_{1-3mm} map in Fig. C.1 and could also be the signature of different dust properties in the outflow compared to the rest of the envelope for this source.

4. Correcting for the central regions

4.1. Applying a sub-arcsec component correction

The central sub-arcsec emission can affect the observed spectral index estimated at larger scales when the analysis is performed in the uv domain, as shown by the work of Miotello et al. (2014) (with unresolved components affecting the emission at all uv distances) and are re-inforced by the tests performed by our team using predictions from synthetic observations of MHD simulations that show that the α_{1-3mm} values of the simulation are recovered for most of the envelope once our central region correction is applied (see Appendix B). If the brightness temperature profiles derived for our sources suggest that the Class 0 envelopes studied in this work are mostly optically thin at mm wavelengths (see Sect. 2.4 and Fig.2), the low β_{1-3mm} values we observe could be due to unresolved optically-thick emission in the central regions of some of our sources but also partly driven by the presence of a central compact component with a different grain population and thus a different emissivity. Moreover, we saw in Sect. 2.3 that on small scales (beyond 200 kλ), the emission could be non-negligibly contaminated by non thermal dust emission, especially at 3.2mm, which would also bias our β_{1-3mm} values. To correct for these contaminations, we subtract the >200 kλ average amplitude from the shorter visibilities at both wavelengths to recalculate corrected β_{1-3mm} values. These average amplitudes are tabulated in Table B.1. Because of the asymmetry of the systems at small scales, we, here again, do not perform the analysis for the two binary sources L1448-N and L1448-2A. We also do not include L1448-C whose 3mm flux

[2] `https://www.iram.fr/IRAMFR/GILDAS/doc/pdf/map.pdf`

[3] In both cases, the emission is resolved out by the interferometers and not linked with a beam elongation

is dominated at most scales studied in this work by the compact component and for which our correction would lead to extremely uncertain β_{1-3mm} values. To take the uncertainties of the correction into account, the corrected β_{1-3mm} values at 500 au and gradients are estimated by generating 2000 sets of radial β_{1-3mm} values varying randomly within their individual error bars following a normal distribution around their nominal value. The corrected β_{1-3mm} values and gradients are provided in Table 2. The orange dashed lines in Fig. 5 indicates the β_{1-3mm} corrected radial trends when the central region correction ('c.r.c') is applied.

Robustness of the correction - We performed a series of tests before choosing our final 200 kλ threshold in order to ensure that our findings were robust. When we subtract 150 kλ average amplitude for instance, we find that most of the sources have the same β_{1-3mm} radial trends. Two sources have a modified slope compared to the 200 kλ correction. SerpS-MM18 has a steeper slope for the 150 kλ correction but the gradient stays within the 40% error bar quoted in Table 2. The second source is L1527 for which a 150 kλ correction leads to a flat beta profile. We note however that the error bar for this source is one of the largest of our sample: the flat β gradient for the 200 kλ correction quoted in Table 2 is also consistent with no gradient at all in this source, within the error bars.

4.2. Impact on the β_{1-3mm} values and radial gradients

After correction, the β_{1-3mm} values at 500 au range from 0.4 to 1.2. The β_{1-3mm} values and radial gradients are not affected in the same way for all the sampled sources. Since a significant correction could be the sign of an optically-thick compact dust emission, we first explore the link with the presence of a disk. Maury et al. (2019) detected candidate disks in all but 4 CALYPSO sources (L1448-2A, L1448-NB1, IRAS4A1 and SerpM-S68N). The disk is resolved for IRAS4B, L1448-C, Serp-MM4 and L1527. In the two sources presenting the largest disk-like structures in the dust emission, namely Serp-MM4 and IRAS4B (radii of 290 and 125 au respectively), we observe that the sub-arcsec correction does not significantly affect our previous estimates. This suggests that there is not a significant difference between the dust properties in the envelope and those obtained integrating over the inner 1″ region. On the contrary, in L1527 (estimated disk radius of 54 au in Maury et al., 2019), the correction is relatively large, suggesting that the small disk could be partially optically thick or host more emissive (thus lower β_{1-3mm}) grains than the envelope. The interpretation is very similar for IRAS2A1: the presence of an unresolved disk (suggested by Maury et al., 2019) with different grain properties could explain the lower β_{1-3mm} values derived before the correction is applied. The 1.3 and 3.2 mm profiles of L1157 and the sub-arcsec correction are very similar to those of L1527. Our results even suggest that the β_{1-3mm} gradient could be reversed once the correction is applied (i.e. with β_{1-3mm} values decreasing toward larger scales), reconciling the gradient estimated in the uv domain with the β_{1-3mm} map derived in the L1157 envelope (see Appendix C and the previously mentioned 3.2 mm extension observed in the outflow direction). For sources with no disk detected in Maury et al. (2019), namely SerpM-S68N and IRAS4A1, we find that those are only weakly affected by our central region correction.

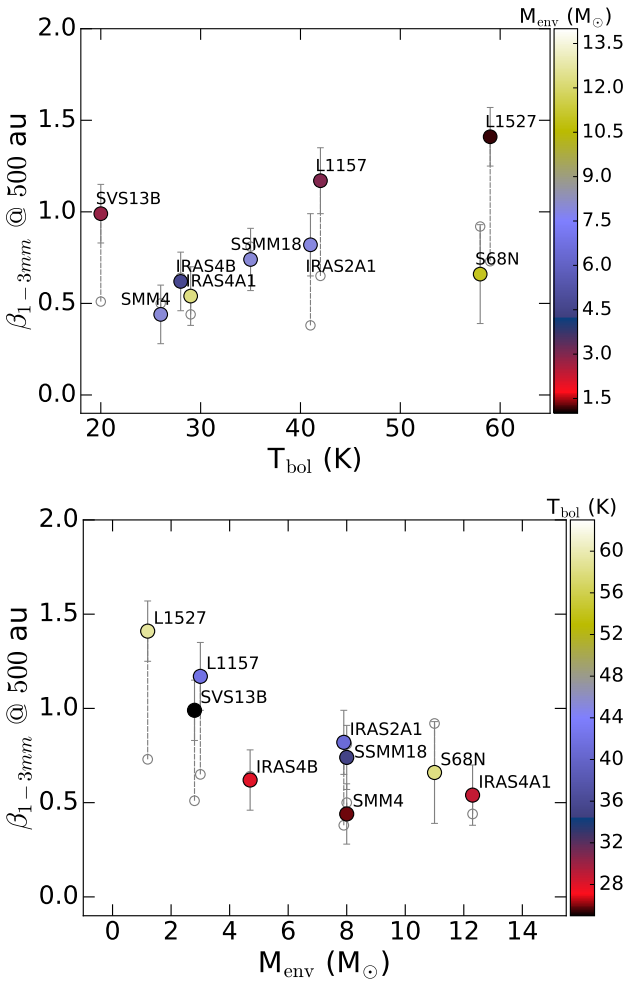

Fig. 6. Relation between the β_{1-3mm} value at 500 au and the bolometric temperature (top) and envelope mass (bottom). The β_{1-3mm} values at 500 au are tabulated in Table 2. Colored/empty symbols represent the values after/before the central region correction.

5. Analysis and discussion

5.1. Does the emissivity index depend on the protostar properties?

The observed β_{1-3mm} values stay low in most of our sources in spite of the central region correction. If in the envelopes of L1157, L1527, and SerpM-S68N, the (corrected) β_{1-3mm} values at 80-2500 au scales mostly stay above 1, the sources IRAS4A, IRAS4B, SVS13, or SerpM-SMM4 have, on average, β_{1-3mm} values below 1 up to 2000 au scales. No correlation was found between the average β_{1-3mm} value and age in a sample of Class I and II objects studied by Ricci et al. (2010). We investigate other correlations in this work. In Fig. 6, we compare the β_{1-3mm} value at 500 au with the bolometric temperatures T_{bol} for each object: the correlation is weak (Pearson correlation coefficient $R = 0.5$) between the two parameters. We note that this result is consistent with the absence of correlation found between the two parameters in the analysis of Froebrich (2005). Like them, we also find an anti-correlation between β_{1-3mm} and M_{env} ($R = -0.79$), which partly suggests smaller grains on average in protostars with smaller envelope mass (Fig. 6). We note that M_{env} estimates strongly depend on the assumed distance and are impacted by the difficulty to separate the envelope from the parent cloud. M_{env} es-

timates are also usually calculated assuming a fixed dust opacity (for instance with $\kappa_{1.3}$, the dust opacity at 1.3 mm fixed to a commonly used value of 0.01 cm^2g^{-1}). This could contribute to the anti-correlation we observed between M_{env} (or N_{H2}) and β_{500au}.

5.2. Steeper emissivity radial evolution in more massive envelopes?

As far as the β_{1-3mm} variations with envelope radius are concerned, IRAS2A1, IRAS4A1, SerpM-SMM4, SerpM-S68N, and SerpS-MM18 present a significant evolution of β_{1-3mm} in their envelopes. All these sources have a relatively large envelope mass ($> 6M_\odot$). We note in particular that the two Serpens sources SerpS-MM18 and SerpM-SMM4 show the same β_{1-3mm} gradient. The sources IRAS4B, SVS13B, L1157, and L1527 have more moderate gradients (< 0.5). Those sources have lower envelope masses than the previous group. In Fig. 7, we show that the steepness of the gradient linking β_{1-3mm} to the envelope scales probed by our observations seems to be strongly correlated to the envelope mass of the object ($R = 0.93$), over an order of magnitude. The relation suggests more homogeneous dust properties in the lowest mass sources of our sample. Note that the more evolved object L1527 presents an homogeneous β_{1-3mm} in its envelope. One explanation could be that the grain populations have been completely mixed over longer timescales.

Investigating more potential relations with environmental properties, we do not find correlations between the β_{1-3mm} gradients with the internal luminosity (Fig. 7), neither do we find steeper β_{1-3mm} gradients in objects presenting larger snowlines nor a correlation between β_{1-3mm} values and the position of the CO snowline itself (Fig. 5; Anderl et al., 2016, Gaudel et al. 2019, sub.).

Complex organic molecules (COMs) are supposedly formed on the surfaces of dust grains and are released in the gas phase when the dust icy mantles sublimate (Rawlings et al., 2013). Belloche et al (in prep) performed a COM analysis for the CALYPSO sample, studying the abundance of molecules such as CH_3OH, C_2H_5OH, CH_3OCH_3, CH_3OCHO, CH_3CHO, NH_2CHO, CH_3CN, C_2H_5CN, a-$(CH_2OH)_2$, $CH_2(OH)CHO$, HNCO or NH_2CN. IRAS2A1, IRAS4B, and SerpS-MM18 have clear detections of most of the cited COMs but do not particularly share a common trend in terms of β_{1-3mm} values or gradients. SerpM-S68N and L1157 both only have CH_3OH, CH_3OCHO and CH_3CN detected but one has the steepest β_{1-3mm} gradient while the other the lowest. The absence of correlation between COM abundances and the radial variations of the dust emissivity index we observe thus suggests that the decrease of the emissivity index at small envelope radii is not driven by the loss of the icy mantles.

Finally, we plot in Fig. 8 the variation of β_{1-3mm} as a function of the dust temperature at the scale it is measured (Eq. 6), allowing a source-to-source local comparison. The large range of β_{1-3mm} values obtained at similar dust temperatures across the sample envelopes suggests that the local dust temperature does not have a major influence on the dust emissivity itself.

5.3. Mm-size grains: can they grow in-situ ... or are they transported?

Several sources have β_{1-3mm} values below 1. Miyake & Nakagawa (1993), Ossenkopf & Henning (1994) or Draine (2006) have shown that grain growth only could already produce $\beta_{1-3mm} \leq 1$ at mm wavelengths. A recent study by Ysard et al. (2019) has quantified the size distribution effects on the shape (peak, β) of the SED of dense interstellar regions including young stellar objects. Their results (see their Fig. 10) clearly show that the mm spectral indices decrease with an increasing size distribution. For most of the material mixtures probed, β values <1 require grain sizes larger than 100 μm.

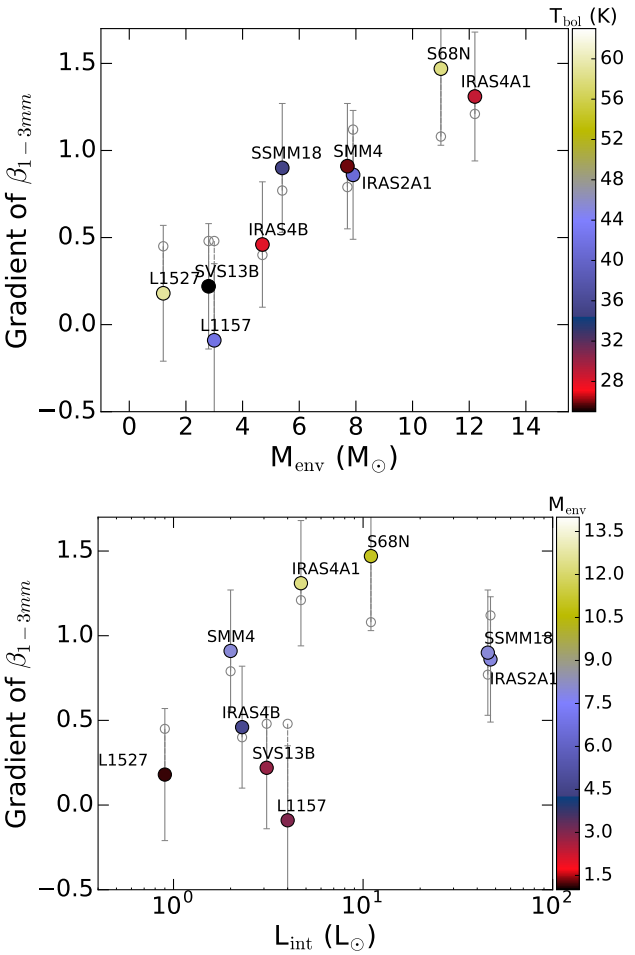

Fig. 7. Relation between the β_{1-3mm} radial gradient and the envelope mass (top) and internal luminosity (bottom). The β_{1-3mm} radial gradients are tabulated in Table 2. Colored/empty symbols represent the values after/before the central region correction.

Many questions remain on how these large grains can form in the youngest protostellar envelopes in spite of the long timescales and high densities required to build them. Ormel et al. (2009) show that long support mechanisms are needed for coagulation to happen and impact the β_{1-3mm} observed in molecular clouds. They find that mm-size particles require ice-coated grains and coagulation times of 10^7 yr to be formed from ISM-like grains, a timescale that shrinks when considering hydrogen number densities $> 10^6$ cm^{-3} (densities that are reached in our protostellar envelopes) or if the coagulation processes start on already grown grains, as expected to explain the coreshine effect observed in cold cores. The denser the medium, the stickier the grains: this enhances the coagulation processes in the inner envelopes during the protostellar collapse.

More recently however, Wong et al. (2016) proposed new coagulation models and found that higher densities ($n_H = 10^{10}$ cm^{-3}) would be required to grow grains above 300 μm in reasonable (a few free-fall time) timescales. To explain the presence of mm-size grains in the Class 0 envelopes, they suggest that large

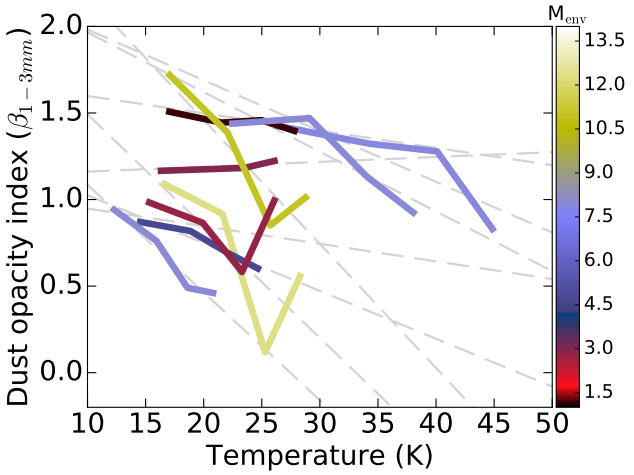

Fig. 8. Local variation of the dust emissivity index $\beta_{1-3\mathrm{mm}}$ as a function of the temperature in the envelope of each source. Lines are color-coded depending on the source envelope mass. The dashed gray lines indicate the fit to the relation for each source, to guide the eye.

grains could be built up in the high-density central region (in the protostellar disk), then be 'launched' into the inner envelope via the gas dragged by the outflow. The transportation conditions would depend on many criteria, for instance the central mass of the stellar embryo (the larger the mass, the less efficient the transportation), the gas velocity (low v_{gas} are needed to transport mm grains), the opening angle of the outflow, its mass loss rate but also the sputtering and shattering rate (namely the ability of a grain to survive gas friction and grain-grain collisions).

Since the outflow momentum flux correlates well with the circumstellar envelope mass (Bontemps et al., 1996), the correlation we observe between M_{env} and the $\beta_{1-3\mathrm{mm}}$ gradient could be linked with stronger outflow energetics in high-mass protostellar envelopes, leading to a more efficient transport of large grains from the inner disk to the inner/intermediate envelope scales. Interestingly, the detection of strongly polarized (from a few percent to up 10%) dust emission at millimeter wavelengths following precisely protostellar outflow cavity walls (Maury et al., 2018, Le Gouellec et al. sub.) suggests a population of large grains (Valdivia et al., 2019) in these specific locations, which strengthen this scenario. The scales on which dust grains could be re-injected in the envelopes using this mechanism as well as the outflow dynamics (gas velocity, grain motions) need to be constrained observationally, especially at the small scales where the outflow is launched and the cavity develops. Current efforts on the theoretical aspects of these investigations, in particular the on-going implementation of the dust grain dynamics into dusty collapse simulations (e.g. Lebreuilly et al., 2019) along with further tests on the decoupling of the dust and gas and potential grains segregation sorting in the equatorial plane (Bate & Lorén-Aguilar, 2017), might provide valuable predictions to carry out additional observational tests in order to constrain the full dust evolution from the core to the disk scales.

5.4. Grain composition effects

The grain chemical composition is expected to vary during the collapse of protostellar envelopes, due to grain-grain collisions, thermal desorption etc. Composition effects could thus also participate in the low β values we observed at mm wavelengths. So far, the very low values of $\beta_{1-3\mathrm{mm}}$ (<<1) have been difficult to explain from optical properties derived in laboratory studies of interstellar dust analogues. Köhler et al. (2015) showed that additional carbonaceous mantles or ices would not lead to such low beta. Studies on magnesium-rich or iron-rich amorphous silicates (Demyk et al., 2017b,a) have shown that the mass absorption coefficient strongly varies with wavelength but the derived mm β values were still higher than 1. Recent work using the optical constants from the THEMIS dust model (Jones et al., 2013) have highlighted the strong influence of the chemical composition on the emission of various mixtures of amorphous hydrogenated carbon grains and amorphous silicates (Ysard et al., 2019). Their study, however, shows that large grains seem to be a necessary condition to explain $\beta_{mm} < 1$. Coupeaud et al. (2011) suggested that astrosilicate grains with a stoichiometry close to that of pyroxene could have $\beta < 1$ in the mm range, with pyroxenes being more abundant, for a given pressure, at lower temperatures (Kessler-Silacci et al., 2005). Several studies of massive protostars as well as protostars from the Orion Molecular Cloud complex seem to confirm that their amorphous silicate population is more dominated by amorphous pyroxene than the typical ISM dust (Demyk et al., 1999; Poteet, 2012). The object-to-object variations of $\beta_{1-3\mathrm{mm}}$ could finally be partly linked with variations in the grain porosity itself (see for instance Kataoka et al., 2014). In conclusions, while a varying grain size distribution remains our favored hypothesis to explain the radial trends we observe, a larger spectrum of laboratory experiments would help predict the observational signatures expected for a variety of interstellar dust analogues and from the collisions of these grains. More observations of the dust polarised emission (and their use as a constraint for polarized dust models) could also bring strong additional information on the dust composition (Guillet et al., 2018).

5.5. Other potential caveats

Studies of 3 mm dust continuum measurements in nearby filaments (Schnee et al., 2014; Mason et al., 2019) recently suggested that the emission at 3 mm deviates from dust emission extrapolated from a simple modified black-body spectral energy distribution (SED) fitted to the shorter wavelengths. The emission is inconsistent with free-free emission or spinning dust models and the enhanced emission at 3 mm has been attributed to the presence of amorphous dust grains. The question on whether 3 mm dust continuum emission can be safely used to study grain size variations in protostellar environments remains, however, open: observations at additional (sub)mm wavelengths but also at higher resolution would enable to sample better the local submm SEDs in order to disentangle between different grains models. Future JWST (James Webb Space Telescope) instruments will also provide the opportunity to observe gases, silicate features (e.g. analyzing the 10-to-18 μm ratio as done in Demyk et al., 1999), or ices in absorption, probing more deeply into the warm interior of the protostellar envelopes.

Galván-Madrid et al. (2018) have recently explored the effects of self-obscuration in protostellar disks with a radially decreasing temperature gradient in producing extremely low spectral indices. Given that most of the emission arising from the Class 0 protostellar envelopes studied in this work is optically thin, our results are probably not affected by these self-obscuration effects.

Finally, our team is currently producing a series of synthetic observations to quantify the impact of various parameters (inclination, size distribution, luminosity, envelope mass) on the observed mm continuum and polarized emission (Valdivia et al. in prep). This work has also been initiated in order to investigate

the instrumental effects linked with interferometric observations and get a better handle on whether they could partly bias the β_{1-3mm} trends we observe.

6. Conclusions

We study the dust properties in a sample of 12 Class 0 protostellar envelopes observed at 94 and 231 GHz with PdBI as part of the CALYPSO survey. We perform our analysis in the visibility domain. We derive dust emissivity index profiles as a function of the envelope scales probed. Since the central arcsec emission can affect the observed spectral index estimated at larger scales, we correct the visibility profiles for this potential contamination. Our analysis leads to the following conclusions:

(i) Most of the Class 0 envelopes present low dust emissivity indices β_{1-3mm}: the observed β_{1-3mm} often reach values lower than 1, in particular in the envelopes of IRAS4A, IRAS4B, SVS13B, and SerpM-SMM4. Many sources also present a strong decrease of β_{1-3mm} toward small envelope radii. Low values of β_{1-3mm} are found preferentially in sources presenting these large radial variations. Both results suggest that grain growth could already be at work in Class 0 inner envelopes.

(ii) The steepness of the β_{1-3mm} gradient depends strongly on the envelope mass, suggesting less grain evolution in low-mass objects and a more diverse grain mixture from the outer to the inner regions in more massive envelopes.

(iii) If accretion and coagulation models do predict the presence of large grains in protostellar envelopes, the timescales required seem to be too large for mm-size grains to be grown directly in the envelopes from ISM-like grains. Potential transportation mechanisms of large grains formed in the high-density inner envelopes and protostellar disks back to the intermediate scales of the envelopes might be able to explain the observations and should be observationally investigated in the future.

(iv) Variation in the grain composition, stoichiometry or porosity also strongly influence the dust emission at mm wavelengths and could partially contribute to the radial trends observed at envelope scales. Recent predictions from a range of interstellar grain mixture analogues suggest however that a certain level of grain growth would still be necessary to explain β_{1-3mm} values <1 (Ysard et al., 2019).

Higher resolution observations, with JWST and ALMA, will help probe deeper into the core and connect the dust properties down to the disk/envelope transition to locally analyze if observations fit with the different accretion, coagulation and transport model predictions.

Acknowledgments

We would first like to thank the referee for their useful comments that help improve the clarity of the paper and robustness of the results. We thank Benoît Commerçon, Karin Demyk, Ugo Lebreuilly, Nathalie Ysard and Vincent Guillet for many fruitful discussions on the analysis, results and interpretation and Jean-Philippe Berger for his help on interferometry related questions. We also thank the CALYPSO collaboration, in particular Sébastien Maret for our discussions on the source distances. This project has received funding from the European Research Council (ERC) under the European Union Horizon 2020 research and innovation programme (MagneticYSOs project, grant agreement N° 679937). LT acknowledges support from the Italian Ministero dell' Istruzione, Università e Ricerca through the grant Progetti Premiali 2012 - iALMA (CUP C52I13000140001), by the Deutsche Forschungs-gemeinschaft (DFG, German Research Foundation) - Ref no. FOR 2634/1 TE 1024/1-1, by the DFG cluster of excellence 'Origins' (`https://www.origins-cluster.de/`), and from the European Union's Horizon 2020 research and innovation programme under the Marie Sklodowska-Curie grant agreement N°823823 (RISE DUSTBUSTERS project).

References

Adams, F. C. 1991, ApJ, 382, 544
Agurto-Gangas, C., Pineda, J. E., Szucs, L., et al. 2019, arXiv: 1901.05021
Anderl, S., Maret, S., Cabrit, S., et al. 2016, A&A, 591, A3
Andersen, M., Steinacker, J., Thi, W. F., et al. 2013, A&A, 559, A60
André, P. 1996, in Astronomical Society of the Pacific Conference Series, Vol. 93, Radio Emission from the Stars and the Sun, ed. A. R. Taylor & J. M. Paredes, 273–284
André, P., Men'shchikov, A., Bontemps, S., et al. 2010, A&A, 518, L102
Andre, P., Ward-Thompson, D., & Barsony, M. 1993, ApJ, 406, 122
André, P., Ward-Thompson, D., & Barsony, M. 2000, Protostars and Planets IV, 59
Anglada, G., Rodriguez, L. F., & Torrelles, J. M. 1996, ApJ, 473, L123
Bate, M. R. & Lorén-Aguilar, P. 2017, MNRAS, 465, 1089
Bazell, D. & Dwek, E. 1990, ApJ, 360, 142
Beckwith, S. V. W. & Sargent, A. I. 1991, ApJ, 381, 250
Beltrán, M. T., Gueth, F., Guilloteau, S., & Dutrey, A. 2004, A&A, 416, 631
Bontemps, S., Andre, P., Terebey, S., & Cabrit, S. 1996, A&A, 311, 858
Bracco, A., Palmeirim, P., André, P., et al. 2017, A&A, 604, A52
Chacón-Tanarro, A., Caselli, P., Bizzocchi, L., et al. 2017, A&A, 606, A142
Chacón-Tanarro, A., Pineda, J. E., Caselli, P., et al. 2019, arXiv e-prints, arXiv:1901.02476
Chen, M. C.-Y., Di Francesco, J., Johnstone, D., et al. 2016, ApJ, 826, 95
Chiang, H.-F., Looney, L. W., & Tobin, J. J. 2012, ApJ, 756, 168
Chiang, H.-F., Looney, L. W., Tobin, J. J., & Hartmann, L. 2010, ApJ, 709, 470
Chini, R., Reipurth, B., Sievers, A., et al. 1997, A&A, 325, 542
Coupeaud, A., Demyk, K., Meny, C., et al. 2011, A&A, 535, A124
Curiel, S., Raymond, J. C., Moran, J. M., Rodriguez, L. F., & Canto, J. 1990, ApJ, 365, L85
D'Alessio, P., Calvet, N., & Hartmann, L. 2001, ApJ, 553, 321
Demyk, K., Jones, A. P., Dartois, E., Cox, P., & D'Hendecourt, L. 1999, A&A, 349, 267
Demyk, K., Meny, C., Leroux, H., et al. 2017a, A&A, 606, A50
Demyk, K., Meny, C., Lu, X. H., et al. 2017b, A&A, 600, A123
Draine, B. T. 2006, ApJ, 636, 1114
Dupac, X., Bernard, J.-P., Boudet, N., et al. 2003, A&A, 404, L11
Eiroa, C., Torrelles, J. M., Curiel, S., & Djupvik, A. A. 2005, AJ, 130, 643
Enoch, M. L., Corder, S., Duchêne, G., et al. 2011, ApJS, 195, 21
Enoch, M. L., Evans, II, N. J., Sargent, A. I., & Glenn, J. 2009, ApJ, 692, 973
Facchini, S., Birnstiel, T., Bruderer, S., & van Dishoeck, E. F. 2017, A&A, 605, A16
Froebrich, D. 2005, ApJS, 156, 169
Fromang, S., Hennebelle, P., & Teyssier, R. 2006, A&A, 457, 371
Galván-Madrid, R., Liu, H. B., Izquierdo, A. F., et al. 2018, ApJ, 868, 39
Gueth, F., Guilloteau, S., Dutrey, A., & Bachiller, R. 1997, A&A, 323, 943
Guillet, V., Fanciullo, L., Verstraete, L., et al. 2018, A&A, 610, A16
Harvey, D. W. A., Wilner, D. J., Myers, P. C., & Tafalla, M. 2003, ApJ, 596, 383
Hsieh, T.-H., Lai, S.-P., & Belloche, A. 2017, AJ, 153, 173
Jones, A. P., Fanciullo, L., Köhler, M., et al. 2013, A&A, 558, A62
Jørgensen, J. K., Bourke, T. L., Myers, P. C., et al. 2007, ApJ, 659, 479
Juvela, M., Demyk, K., Doi, Y., et al. 2015, A&A, 584, A94
Kaas, A. A., Olofsson, G., Bontemps, S., et al. 2004, A&A, 421, 623
Karska, A., Herczeg, G. J., van Dishoeck, E. F., et al. 2013, A&A, 552, A141
Kataoka, A., Okuzumi, S., Tanaka, H., & Nomura, H. 2014, A&A, 568, A42
Kern, N. S., Keown, J. A., Tobin, J. J., Mead, A., & Gutermuth, R. A. 2016, AJ, 151, 42
Kessler-Silacci, J. E., Hillenbrand, L. A., Blake, G. A., & Meyer, M. R. 2005, ApJ, 622, 404
Köhler, M., Ysard, N., & Jones, A. P. 2015, A&A, 579, A15
Kristensen, L. E., van Dishoeck, E. F., Bergin, E. A., et al. 2012, A&A, 542, A8
Kruegel, E. & Siebenmorgen, R. 1994, A&A, 288, 929
Kwon, W., Fernández-López, M., Stephens, I. W., & Looney, L. W. 2015, ApJ, 814, 43
Kwon, W., Looney, L. W., Mundy, L. G., Chiang, H.-F., & Kemball, A. J. 2009, ApJ, 696, 841

Lebreuilly, U., Commerçon, B., & Laibe, G. 2019, A&A, 626, A96
Lefèvre, C., Pagani, L., Juvela, M., et al. 2014, A&A, 572, A20
Li, J. I., Liu, H. B., Hasegawa, Y., & Hirano, N. 2017, ApJ, 840, 72
Lugo, J., Lizano, S., & Garay, G. 2004, ApJ, 614, 807
Martin, P. G., Roy, A., Bontemps, S., et al. 2012, ApJ, 751, 28
Mason, B., Dicker, S., Sadavoy, S., et al. 2019, arXiv e-prints, arXiv:1905.05221
Mathis, J. S., Rumpl, W., & Nordsieck, K. H. 1977, ApJ, 217, 425
Maury, A. J., André, P., Men'shchikov, A., Könyves, V., & Bontemps, S. 2011, A&A, 535, A77
Maury, A. J., André, P., Testi, L., et al. 2019, A&A, 621, A76
Maury, A. J., Girart, J. M., Zhang, Q., et al. 2018, MNRAS, 477, 2760
McMullin, J. P., Mundy, L. G., Wilking, B. A., Hezel, T., & Blake, G. A. 1994, ApJ, 424, 222
Meehan, L. S. G., Wilking, B. A., Claussen, M. J., Mundy, L. G., & Wootten, A. 1998, AJ, 115, 1599
Melis, C., Duchêne, G., Chomiuk, L., et al. 2011, ApJ, 739, L7
Miotello, A., Testi, L., Lodato, G., et al. 2014, A&A, 567, A32
Miyake, K. & Nakagawa, Y. 1993, Icarus, 106, 20
Motte, F. & André, P. 2001, A&A, 365, 440
Motte, F., Andre, P., & Neri, R. 1998, A&A, 336, 150
Natta, A., Testi, L., Calvet, N., et al. 2007, in Protostars and Planets V, ed. B. Reipurth, D. Jewitt, & K. Keil, 767
Ormel, C. W., Paszun, D., Dominik, C., & Tielens, A. G. G. M. 2009, A&A, 502, 845
Ortiz-León, G. N., Loinard, L., Dzib, S. A., et al. 2018a, ApJ, 865, 73
Ortiz-León, G. N., Loinard, L., Dzib, S. A., et al. 2018b, ApJ, 869, L33
Ossenkopf, V. 1993, A&A, 280, 617
Ossenkopf, V. & Henning, T. 1994, A&A, 291, 943
Pagani, L., Steinacker, J., Bacmann, A., Stutz, A., & Henning, T. 2010, Science, 329, 1622
Pascucci, I., Gorti, U., & Hollenbach, D. 2012, ApJ, 751, L42
Pérez, L. M., Carpenter, J. M., Chandler, C. J., et al. 2012, ApJ, 760, L17
Pérez, L. M., Chandler, C. J., Isella, A., et al. 2015, ApJ, 813, 41
Planck Collaboration, Abergel, A., Ade, P. A. R., et al. 2014, A&A, 571, A11
Plunkett, A. L., Fernández-López, M., Arce, H. G., et al. 2018, A&A, 615, A9
Poteet, C. A. 2012, PhD thesis, The University of Toledo
Rawlings, J. M. C., Williams, D. A., Viti, S., Cecchi-Pestellini, C., & Duley, W. W. 2013, MNRAS, 430, 264
Reipurth, B., Rodríguez, L. F., Anglada, G., & Bally, J. 2002, AJ, 124, 1045
Reissl, S., Wolf, S., & Brauer, R. 2016, A&A, 593, A87
Ricci, L., Testi, L., Natta, A., & Brooks, K. J. 2010, A&A, 521, A66
Robitaille, T. P., Whitney, B. A., Indebetouw, R., Wood, K., & Denzmore, P. 2006, ApJS, 167, 256
Rodríguez, L. F., Anglada, G., & Curiel, S. 1997, ApJ, 480, L125
Sadavoy, S. I., Di Francesco, J., Andre, P., et al. 2014, ApJ, 787, L18
Sadavoy, S. I., Stutz, A. M., Schnee, S., et al. 2016, A&A, 588, A30
Schnee, S., Mason, B., Di Francesco, J., et al. 2014, MNRAS, 444, 2303
Steinacker, J., Andersen, M., Thi, W. F., et al. 2015, A&A, 582, A70
Steinacker, J., Pagani, L., Bacmann, A., & Guieu, S. 2010, A&A, 511, A9
Tazzari, M., Testi, L., Ercolano, B., et al. 2016, A&A, 588, A53
Terebey, S., Chandler, C. J., & Andre, P. 1993, ApJ, 414, 759
Testi, L., Birnstiel, T., Ricci, L., et al. 2014, in Protostars and Planets VI, ed. H. Beuther, R. S. Klessen, C. P. Dullemond, & T. Henning, 339
Testi, L., Natta, A., Shepherd, D. S., & Wilner, D. J. 2001, ApJ, 554, 1087
Testi, L., Natta, A., Shepherd, D. S., & Wilner, D. J. 2003, A&A, 403, 323
Teyssier, R. 2002, A&A, 385, 337
Tobin, J. J., Dunham, M. M., Looney, L. W., et al. 2015, ApJ, 798, 61
Tobin, J. J., Hartmann, L., Chiang, H.-F., et al. 2013, ApJ, 771, 48
Tobin, J. J., Looney, L. W., Li, Z.-Y., et al. 2016, ApJ, 818, 73
Torres, R. M., Loinard, L., Mioduszewski, A. J., & Rodríguez, L. F. 2009, ApJ, 698, 242
Tychoniec, Ł., Tobin, J. J., Karska, A., et al. 2018a, ApJ, 852, 18
Tychoniec, Ł., Tobin, J. J., Karska, A., et al. 2018b, ApJS, 238, 19
Valdivia, V., Maury, A., Brauer, R., et al. 2019, MNRAS, 488, 4897
Whitney, B. A., Wood, K., Bjorkman, J. E., & Wolff, M. J. 2003, ApJ, 591, 1049
Wong, Y. H. V., Hirashita, H., & Li, Z.-Y. 2016, PASJ, 68, 67
Ysard, N., Koehler, M., Jimenez-Serra, I., Jones, A. P., & Verstraete, L. 2019, arXiv e-prints, arXiv:1909.05015
Zucker, C., Speagle, J. S., Schlafly, E. F., et al. 2019, arXiv:1902.01425

Appendix A: Free-free and synchrotron contributions to the 1.3 and 3.2 mm emission

In order to quantify the contribution to the PdBI observations not coming from thermal dust emission, we assume that the $\geq$ 2 cm emission can be considered as free from thermal dust emission (as observed in IRAS2A by Tobin et al., 2015) and considered as compact. We gather fluxes beyond 2 cm published in the literature. For sources with more than two observational constraints, we estimate the free-free + synchrotron spectral slope $\alpha_{\rm ff+s}$ as:

$$F_\lambda \propto (\lambda/\lambda_0)^{-\alpha_{\rm ff+s}} \quad \text{(A.1)}$$

with λ_0 = 1 mm. We then extrapolate the fitted spectrum to the mm regime and compare it with the 1.3 and 3.2 mm PdBI fluxes at 200 kλ (so on our smallest scales) to estimate the contamination at both wavelengths. The references of the used radio fluxes, the derived $\alpha_{\rm ff+s}$ slopes and the contamination to the 1.3 and 3.2 mm emission are reported in Table A.1. For SerpM-SMM4 where only the 3.6 cm flux was found, we fix $\alpha_{\rm ff+s}$ to 1.1, which is the $\alpha_{\rm ff+s}$ value of IRAS4A1, the source in the sample that is the closest in terms of envelope mass, temperature and internal luminosity. For SerpS-MM18, the $\alpha_{\rm ff+s}$ value was derived by Kern et al. (2016) from observations at 4.75 and 7.25 GHz. We note that several mm sources reside in the 4″ beam, as observed in Plunkett et al. (2018). The high $\alpha_{\rm ff+s}$ found by Kern et al. (2016) (∼2-2.3) suggests that thermal dust emission might still contribute to the cm emission. As in SerpM-SMM4, we decided to fix $\alpha_{\rm ff+s}$ to 1.1 for this source. The contribution is systematically lower than 10% at 1.3 mm, but it can become non negligible at 3.2 mm. Calculated using the radio sources of Kern et al. (2016) for SerpS-MM18, the contamination accounts for all the 200 kλ 1.3 and 3.2mm fluxes, with a large $\alpha_{\rm ff+s}$ (> 2) usually associated with optically thick emission.

Appendix B: Predictions from synthetic observations: a noticeable impact of the central region

The observations have shown that analysis of the spectral index performed in the uv domain can be biased by unresolved optically-thick emission or the presence of central compact components. We subtracted the >200 kλ average amplitude to correct for these contaminations. These average amplitudes are tabulated in Table B.1. In order to further test the effects of this correction on the 1.3 and 3.2 mm visibility profiles and deduced $\beta_{1-3\rm mm}$, we generate synthetic observations starting from a non-ideal MHD simulation of the gravitational collapse of a pre-stellar core. The simulation is generated using the RAMSES code (Teyssier, 2002; Fromang et al., 2006). The core has a mass of 2.5 $M_\odot$, a mass-to-flux ratio μ = 6 and a rotational to gravitational energy ratio of 10^{-2}. The effective resolution is ∼ 1 au. More details on this simulation are provided in Valdivia et al. (2019) (see also Maury et al., 2018). We select a snapshot where the central embryo has accreted 0.2 $M_\odot$ and post-process a zoomed-in region of 8000 au using the radiative transfer code POLARIS (Reissl et al., 2016, POLArized RadIation Simulator;). We assume a gas-to-dust mass ratio of 100 and a MRN-like (Mathis et al., 1977) dust grain size distribution (n(a) $\propto a^{-3.5}$; 5 nm $\leq$ a $\leq$ 1 μm). The composition is 62.5% astronomical silicates and 37.5% carbonaceous grains: the simulation neither includes dust evolution, nor dust dynamics. The chosen accretion luminosity and distance are 1$L_\odot$ and 120 pc respectively. Figure B.1 shows the integrated dust emission of the protostellar envelope at 1.3 and 3.2 mm, with a density distribution close to a simple power law, a pseudo-disk and bipolar outflow bubbles extending to up to 800 au. We show how the predicted spectral index (Eq. 2) varies locally in the synthetic envelope in the bottom panel, with $\alpha \sim 3$ in the outer part of the envelopes,

Table A.1. Upper limits on the contribution to the 1.3 and 3.2 mm emission not coming from thermal dust emission

Name	$\alpha_{\rm ff+s}$ [a]	Flux @ 200 kλ at 1.3 mm (mJy)	Contribution at 1.3 mm (%)	Flux @ 200 kλ at 3.2 mm (mJy)	Contribution at 3.2 mm (%)	References [b]
NGC1333-IRAS2A1	1.1	85	4.5	13	11	1
NGC1333-IRAS4A1	1.1	310	3.8	47	9.1	3
NGC1333-IRAS4B	0.5	196	0.2	20	1.4	3
L1448-2A	0.5	28	4.0	3.9	18	3
L1448-C	1.0	102	2.9	18	6.7	3
L1448-NB1	0.3	82	3.6	13	14	2, 4
SVS13B	0.8	72	6.9	12	19	5
L1527	0.3	136	1.7	19	9.3	6
SerpM-S68N	0.6	45	0.9	3.4	6.8	7,8
SerpM-SMM4	1.1 *(f)*	46	9.6	8.7	19	8
SerpS-MM18	1.1 *(f)*	97	3.6	8.2	16	9
L1157	0.3	103	0.5	12.6	3.2	10

[a] As in Tobin et al. (2015), the spectral slopes $\alpha_{\rm ff+s}$ are defined by $F_\nu = F_0(\lambda/\lambda_0)^{-\alpha_{\rm ff+s}}$, with λ_0 = 1 mm. *(f)* indicates when $\alpha_{\rm ff+s}$ has been fixed to 1.1.

[b] References for the cm fluxes used to estimate the free-free+synchrotron contribution: [1] Tobin et al. (2015), [2] Reipurth et al. (2002), [3] Tychoniec et al. (2018b), [4] Curiel et al. (1990), [5] Rodríguez et al. (1997), [6] Melis et al. (2011), [7] McMullin et al. (1994), [8] Eiroa et al. (2005), [9] Kern et al. (2016), [10] Meehan et al. (1998).

Table B.1. Average amplitude for >200 kλ baselines

Name	$F^{1.3mm}_{>200k\lambda}$ (mJy)	$F^{3.2mm}_{>200k\lambda}$ (mJy)
IRAS2A1	85.4	13.3
IRAS4A1	309.6	47.2
IRAS4B	196.1	20.0
SVS13B	71.8	12.4
L1527	135.6	18.9
SerpM-S68N	45.2	3.4
Serp-SMM4	83.8	8.7
SerpS-MM18	97.4	8.2
L1157	103.0	12.6

increasing up to 3.3 in the outflow bubble, then decreasing drastically below 2 in the central 50 au where an optically-thick disk component resides.

The 1.3 and 3.2 mm emission maps are used as inputs for the ALMA simulator of the `CASA`[4] software. We run the *simobserve* task to produce 4 simulated measurement sets for compact and extended ALMA antenna configurations, C43-1, C43-3, C43-5, and C43-8[5]. We use integration times of 7200s per configuration and assume a PWV of 0.7 mm (i.e. under good atmospheric conditions). Thermal noise (default ATM model) is added to the simulated data. We then extract the concatenated visibilities using `GILDAS/MAPPING`. Figure B.2 shows the predicted observations in the uv domain at 1.3 and 3.2 mm and their associated spectral indices α. The α values plunging at small scales can be explained by the central (∼50 au) region that, with its weak ($\alpha < 3$) values, affects the whole visibility profile. To correct for this contribution, we mask the inner region : we calculate the fluxes at 1.3 and 3.2 mm at 200 kλ (to be sure to encompass the 50 au central region) and remove them from the visibility amplitudes at all shortest baselines. The corrected trend for α is overlaid in Fig. B.2 (dashed blue line). The $\alpha \geq 3$ values observed in the α map (Fig. B.1 bottom) are recovered for most of the envelope, with a nearly constant α after the correction. We also re-run the tests using a simulation where the temperature is fixed to 10 K during the post-processing but this does not affect our results: we conclude that temperature gradients along the line of sight should only have a minor effect on our results.

[4] https://casa.nrao.edu/

[5] The configuration files are retrieved from https://almascience.nrao.edu/tools/casa-simulator.

Appendix C: Maps of $\beta_{1-3\rm mm}$

For a qualitative assessment of the spatial variations of the dust emissivity index $\beta_{1-3\rm mm}$, we perform an imaging of the dust continuum emission (including the secondary sources) using `GILDAS/MAPPING`. We apply a robust weighting scheme, compromise between the natural weighting and the uniform weighting that minimizes in particular the synthesized beam sides lobes. Table C.1 provides the synthesized beam and the rms of the obtained 94 and 231 GHz maps. In order to build maps of $\beta_{1-3\rm mm}$, we need to have both 94 and 231 GHz maps tracing the same physical scales at the same resolution. We thus apply an additional uv tapering on the visibilities at 231 GHz in order to obtain beams at 231 GHz similar (in size and orientation) to those at 94 GHz. Maps are produced with the same pixel size. The 'tapered' sizes and rms of these new maps are also given in Table C.1 (231 GHz-tapered columns). We finally use the temperature profiles estimated for each source to apply Eq. 7 on a pixel-by-pixel basis. Figure C.1 shows the $\beta_{1-3\rm mm}$ maps of the sample. $\beta_{1-3\rm mm}$ is shown at locations where the emission at 1.3 and 3.2 mm is detected with a signal-to-noise ratio higher than two. We observe that the dust emissivity index changes in the envelopes of most of the sources as observed in the uv domain. However, when $\beta_{1-3\rm mm}$ values are averaged over various aperture sizes, we observe that $\beta_{1-3\rm mm}$ gradients are not as clearly observed as one probes smaller and smaller scales compared to the results obtained from the uv domain analysis. This demonstrates the difficulty to analyze $\beta_{1-3\rm mm}$ spatial variations directly from interferometric maps affected by filtering.

Table C.1. Characteristics of the dust continuum maps shown in Fig.C.1

Name	Synthesized beams		rms (Jy/beam)	
	94 GHz	231 GHz-tapered	94 GHz	231 GHz-tapered
IRAS2A1	1.″45 × 1.″02 (38°)	1.″40 × 1.″06 (35°)	1.71×10^{-4}	4.04×10^{-3}
IRAS4A1	1.″58 × 1.″02 (-155°)	1.″59 × 0.″93 (26°)	1.03×10^{-3}	1.26×10^{-2}
IRAS4B	1.″57 × 1.″01 (25°)	1.″53 × 0.″96 (25°)	1.33×10^{-3}	9.31×10^{-3}
L1448-2A	1.″47 × 0.″96 (43°)	1.″43 × 0.″99 (44°)	6.27×10^{-5}	8.23×10^{-4}
L1448-C	1.″52 × 0.″99 (42°)	1.″52 × 0.″99 (45°)	9.79×10^{-5}	1.82×10^{-3}
L1448-NB1	1.″49 × 1.″02 (35°)	1.″46 × 1.″00 (37°)	2.60×10^{-4}	6.37×10^{-3}
SVS13B	1.″58 × 1.″00 (24°)	1.″58 × 0.″98 (25°)	2.13×10^{-4}	6.61×10^{-3}
L1527	1.″56 × 1.″05 (35°)	1.″54 × 1.″06 (36°)	7.52×10^{-5}	1.89×10^{-3}
SerpM-S68N	1.″69 × 0.″89 (29°)	1.″69 × 0.″91 (30°)	8.28×10^{-5}	1.42×10^{-3}
SerpM-SMM4	1.″75 × 0.″88 (28°)	1.″79 × 0.″98 (29°)	2.02×10^{-4}	5.16×10^{-3}
SerpS-MM18	1.″71 × 0.″84 (27°)	1.″71 × 0.″92 (24°)	2.18×10^{-4}	5.43×10^{-3}
L1157	1.″41 × 1.″09 (62°)	1.″47 × 1.″01 (61°)	9.23×10^{-5}	1.80×10^{-3}

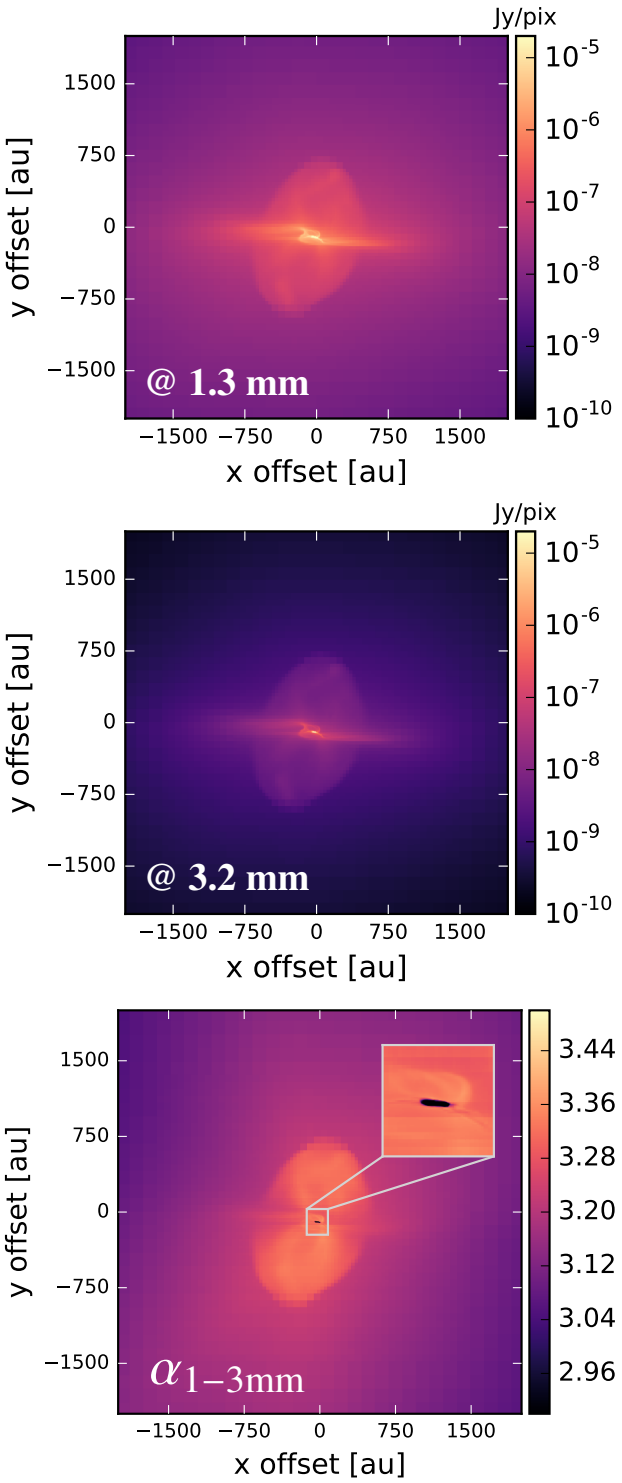

Fig. B.1. *Top two panels:* Synthetic observations at 1.3 and 3.2 mm of the core-collapse simulation used in this analysis. The radiative transfer is performed using the POLARIS code. The flux is in Jy/pixel. The pixel size is 1 au. *Bottom:* Spectral indices α_{1-3mm} derived from the simulation. α_{1-3mm} is defined as log ($F_{\nu 0}$ / $F_{\nu 1}$) / log ($\nu 0$ / $\nu 1$), with $\nu 0$ and $\nu 1$ being 231 and 94 GHz respectively
. The inset shows a zoom on the central 200 au region.

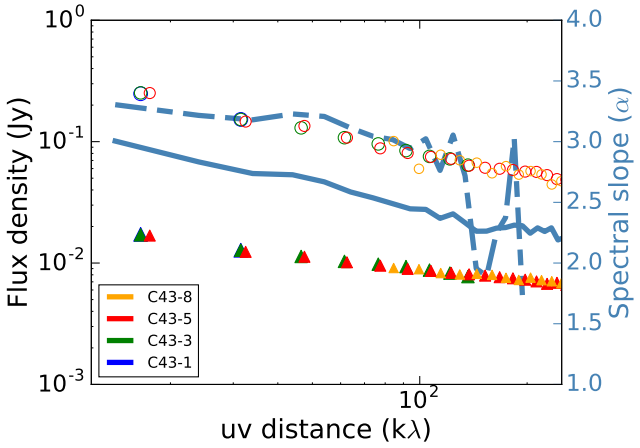

Fig. B.2. Predicted flux density of the dust continuum at 1.3 mm (open circles) and 3.2 mm (filled triangles) as a function of the uv distance averaged every 25 kλ for different ALMA antenna configurations. The corresponding spectral index α is shown with the blue plain line. Values are given on the right y-axis. The dashed blue line indicates α values corrected for the central regions (average flux around 200 kλ removed).

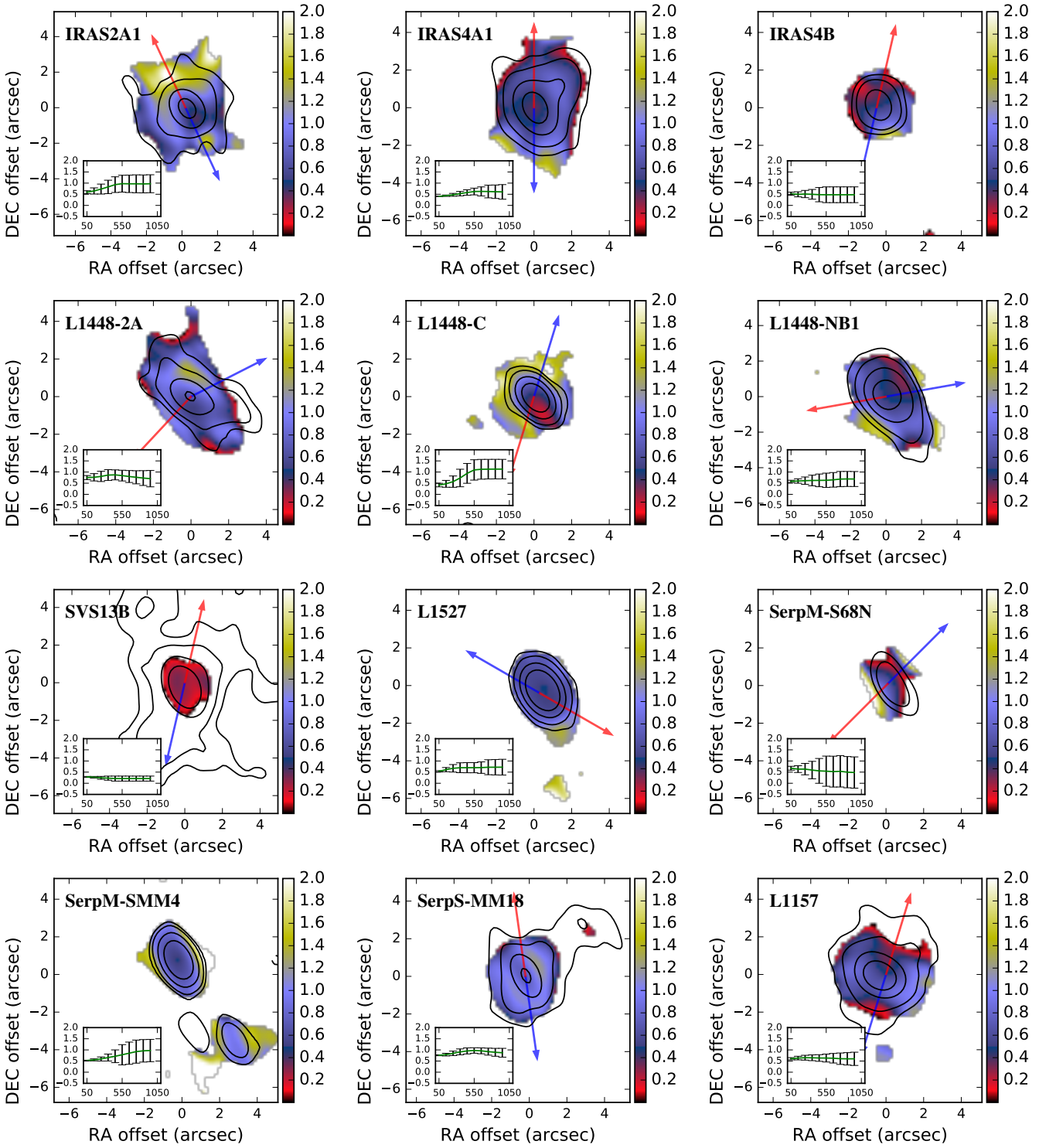

Fig. C.1. Maps of the dust emissivity index β_{1-3mm}. Only pixels with a 2-σ detection at both wavelengths are displayed. The contours indicate the 94 GHz emission detected at 3, 5, 10, 30, and 80-σ. The blue and red arrows indicate the direction of the bipolar jets. The insets show how β_{1-3mm} evolves as values get integrated to larger and larger scales. The x-axis of the inset plots is labeled in au.